Surfaces and Interfaces 26 (2021) 101369

Contents lists available at ScienceDirect

Surfaces and Interfaces

journal homepage: www.sciencedirect.com/journal/surfaces-and-interfaces

# Epitaxially grown copper phosphide ($Cu_3P$) nanosheets nanoarchitecture compared with film morphology for energy applications

Suk Woo Lee [a,b], Jaemin Kim [a,b], Sang-Gil Woo [c], Youngjin Park [a,d], Jong Chan Yoon [a,b], Hyo Ju Park [a], Na Yeon Kim [a], Hyeon Suk Shin [a,d], Zonghoon Lee [a,b,*]

[a] Center for Multidimensional Carbon Materials, Institute for Basic Science (IBS), Ulsan 44919, South Korea
[b] Department of Materials Science and Engineering, Ulsan National Institute of Science and Technology (UNIST), Ulsan 44919, South Korea
[c] Advanced Batteries Research Center, Korea Electronics Technology Institute (KETI), Geonggi-do 13509, Seongnam, South Korea
[d] Department of Chemistry, Ulsan National Institute of Science and Technology (UNIST), Ulsan 44919, South Korea

ARTICLE INFO

*Keywords:*
Epitaxial growth
Nanoarchitecture
Copper phosphide ($Cu_3P$)
Transition metal phosphide
Li-ion battery
Hydrogen evolution reaction

ABSTRACT

Fabrication of 3D nanoarchitecture is one of the effective ways to improve performance of energy applications because it has advantages such as buffer space accommodating volume expansion or high surface area leading to higher efficiency. However, the fabrication of such nanoarchitectures is generally complex involving several steps including patterning, etching and growth of intermediate materials. Herein, we report a facile process to form a nanoarchitecture of copper phosphide ($Cu_3P$) nanosheets directly on copper foil by epitaxially growing $Cu_3P$ sheets of controlled thickness on a suitably engineered Cu foil. The growth of $Cu_3P$ nanosheets and their epitaxial relationship with the Cu foil were studied by X-ray diffraction (XRD) and transmission electron microscopy (TEM). To show the advantages of nanoarchitecture, we tested both nanoarchitecture and film-like morphology of $Cu_3P$ as an anode in lithium-ion battery (LIB) and an electrocatalyst in hydrogen evolution reaction (HER). We found that the nanoarchitecture enabled significant improvements in both capacity and rate capability of the LIB. In the case of HER, however, the higher electrocatalytic efficiency of the nanoarchitectured electrode was maintained only in the initial cycles due to morphology reconstruction of $Cu_3P$ during HER. This result provides a new facile route to fabricate nanoarchitecture and shows superior performance of the nanoarchitecture in energy applications.

## 1. Introduction

In recent times, transition metal phosphides (TMPs) have been investigated in energy applications, namely, as anodes for lithium ion batteries (LIB) and as electrocatalysts in hydrogen evolution reaction (HER), oxygen evolution reaction (OER), or hydrazine oxidation reaction (HzOR) [1–4]. TMPs are considered to be among the potential candidate of anode materials in LIB anodes due to their higher gravimetric and volumetric capacities than graphite, which is currently the most widely used LIB anode [5–7]. In HER and OER, TMPs are increasingly being used as acid-stable and active catalysts to replace scarce and expensive noble metals [8–10]. Even so, the performance of TMPs in actual energy applications currently remains lower than expected. This has been attributed mainly to contact problems between the TMP active material and the metal current collector of the anode. A conductive binder adhesive is used to attach the TMP to the metal which often leads to capacity loss by inhibiting ion transport from the electrolyte [11,12]. To circumvent this problem, the direct growth of TMPs on the current collector has been extensively investigated. Another issue that critically affects performance is the architecture of the TMP anode since LIB anodes based on TMPs undergo significant volume changes during charge and discharge cycles resulting in detachment or elimination of TMPs from the current collector thus deteriorating the performance of the LIB [13,14]. For the application of TMPs in HER, a high surface area to maximize contact with the electrolyte is necessary for high electrocatalytic efficiency [15,16]. Consequently, different morphologies including nanosheet, nanopillars, nanoparticle, and porous architectures of TMPs have been designed both to increase buffer space to accommodate volume changes and high surface area for optimal electrocatalytic efficiency [1,5,17,18]. However, the fabrication of these complex architectures on the current collector involves laborious additional treatments in the form of patterning, etching or growing an

* Corresponding author.
*E-mail address:* zhlee@unist.ac.kr (Z. Lee).

https://doi.org/10.1016/j.surfin.2021.101369
Received 20 May 2021; Received in revised form 12 July 2021; Accepted 21 July 2021
Available online 3 August 2021

intermediate such as CuOH [4,5,9,18]. Hence, the direct fabrication of the desired TMPs nanoarchitecture on the current collector is highly desirable.

Herein, we report the direct and epitaxial growth of copper phosphide ($Cu_3P$) nanosheets, which is one of TMPs, on a copper (Cu) foil by a solid-vapor reaction. The thickness of the $Cu_3P$ nanosheet was varied from 30 nm–400 μm by controlling the chamber pressure during growth. Interestingly, the as-grown $Cu_3P$ nanosheets were found to be vertically aligned on the Cu foil. Transmission electron microscopy (TEM) and X-ray diffraction (XRD) results revealed that this alignment is due to an epitaxial relation between $Cu_3P$ and Cu. We found that through epitaxial growth and controlling the nanosheet thickness, a nanoarchitecture of $Cu_3P$ nanosheets was directly fabricated on the Cu foil in a single step without any additional treatment. Comparing with film-like morphology of $Cu_3P$, we tested the $Cu_3P$ nanoarchitecture as anode in a LIB and for the HER. The $Cu_3P$ anode with nanoarchitecture showed higher capacity and rate capability in LIB as compared to $Cu_3P$ with a film-like morphology. However, for the HER, the electrocatalytic efficiency of the nanoarchitecture was higher only in the first cycle after which, the performance decreased due to morphology reconstruction of $Cu_3P$ during operation.

## 2. Material and methods

### 2.1. Fabrication of copper phosphide ($Cu_3P$) with nanostructured architecture on Cu foil

The Cu foil (99.8%, Alfa Aesar) was annealed based on a reported method to produce large domain size crystallographic planes with predominantly the (200) plane on the surface [19]. The Cu foil was heated up to 1000 °C in 5 mTorr and then annealed for 30 min without additional gas. After that, 2 sccm of $H_2$ gas was introduced and additionally annealed for 30 min. The annealed Cu foil was placed in a tube furnace along with 0.2 g red phosphorus (> 97 %, Sigma-Aldrich); the Cu foil was at a distance of 15 cm from the red phosphorous. The tube furnace was heated at 300 °C for 2 h to form $Cu_3P$. Growth was carried out for different chamber pressures with Ar carrier gas which flow rate was varied from 0 to 50 sccm for each chamber pressure. A schematic of the process is shown in Fig. 1.

### 2.2. Characterization

Scanning electron microscopy (SEM) images were taken with Hitachi S-4800 microscope and X-ray photoelectron spectroscopy (XPS) was carried out by Thermo Fisher K-alpha system. X-ray diffraction (XRD) patterns were obtained using Rigaku D/Max2500V with 1.5406 Å Cu Kα radiation. Transmission electron microscopy (TEM), high-angle annular dark-field scanning transmission electron microscopy (HAADF-STEM) and selected area electron diffraction (SAED) were carried out with JEOL JEM-2100F equipped with a Cs probe corrector at the accelerating voltage of 200 kV. Cross-sectioned TEM samples were prepared using a focused ion beam (FIB) instrument (FEI Quanta 3D FEG) equipped with an electron backscattered diffraction (EBSD) detector that allowed to determine grain sizes and crystallographic planes of the Cu foil substrates.

### 2.3. Electrochemical measurements

For the electrochemical measurements, we used similar mass of $Cu_3P$ (~2.6 mg) on 4 $cm^2$ of Cu foil for all growth condition. To investigate the rate capability of $Cu_3P$-5 and $Cu_3P$-300, the half cells (CR2032) were prepared as follows. The cells were assembled using synthesized samples as a working electrode, polypropylene as a separator, lithium foil as the counter electrode, and 1 M $LiPF_6$ in ethylene carbonate (EC)/ethyl methyl carbonate (EMC) (3:7 v/v) as the electrolyte (provided by PanaxEtec). The charge-discharge experiments were performed galvanostatically over a voltage range of 0.02–3 V vs. $Li^+/Li$ with different currents at room temperature. (1C = 363 $mAhg^{-1}$). Electrocatalytic measurements were carried out using a 3-electrode cell and a 0.5 M sulfuric acid ($H_2SO_4$) electrolyte solution. Graphite rod (Sigma Aldrich) as a counter electrode and Ag/AgCl reference electrode were used. Grown $Cu_3P$ samples were directly used to measure electrocatalytic measurements. The linear sweep voltammetry was performed with 10 mV/s scan rate using a potentiostat (Zive SP2, ZIVE LAB).

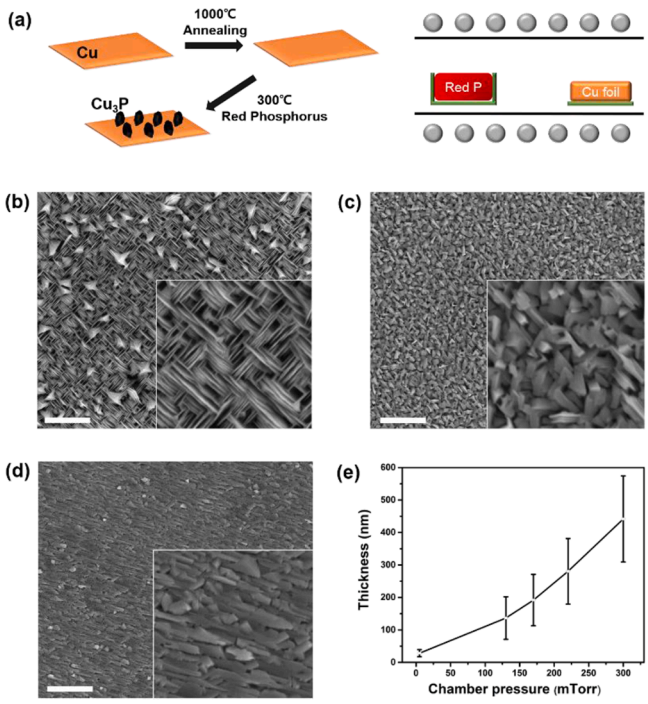


**Fig. 1.** (a) Schematic diagram showing the formation of $Cu_3P$ nanoarchitecture on annealed Cu foil, and the tube furnace used for heating Cu foil with red phosphorous. (b–d) SEM images of $Cu_3P$ architectures under (b) 5 ($Cu_3P$-5), (c) 170 ($Cu_3P$-170) and (d) 300 mTorr ($Cu_3P$-300) chamber pressure. Scale bars are 5 μm. (e) Variation of $Cu_3P$ nanosheet thickness with chamber pressure.

## 3. Result and discussion

$Cu_3P$ was grown by the reaction of red phosphorus with the annealed Cu foil. During the heat treatment, red phosphorus vaporized and reacted with the surface of the Cu foil to form $Cu_3P$. We tested the growth of $Cu_3P$ at different chamber pressures (5, 170, 220, and 300 mTorr) to investigate effect of pressure on $Cu_3P$ growth (Fig. 1).

Fig. 1b-d show SEM images of $Cu_3P$ sheets grown at different pressures of 5, 170 and 300 mTorr. It is clearly seen that the thickness of $Cu_3P$ sheets depends on the chamber pressure; the thickness increased from ~ 28 nm to ~440 μm with increase in pressure. At 5 mTorr pressure, a nanoarchitecture is formed ($Cu_3P$-5 in Fig. 1b), whereas the morphology is more film-like at 300 mTorr ($Cu_3P$-300 in Fig. 1d). However, the sheet morphology of $Cu_3P$ is consistently maintained regardless of thickness. We attribute the formation of nanosheets to the difference in growth rate of different $Cu_3P$ facets due to varying surface stability. To quantify this effect, we calculated the density of dangling bonds (which is related to the surface stability for a crystalline facet [20]), based on a previously reported bonding configuration of $Cu_3P$ [21] (Table 1 and supplementary Fig. S1). In the bonding configuration considered, the density of dangling bonds (DBs) for the (001) and (100) planes are 32.41 and 51.59/$nm^2$, respectively. The lower DB density of the (001) plane implies that this plane has a higher surface stability than the (100) plane indicating that growth perpendicular to (001) is slower than that perpendicular to (100). This difference in growth rate between

**Table 1**
The number and density of dangling bonds (DB) in (001) and (100) planes of $Cu_3P$.

| | (001) plane | (100) plane |
|---|---|---|
| Plane Area | 0.432 $nm^2$ | 0.504 $nm^2$ |
| The number of dangling bonds | 14 | 26 |
| Density of dangling bonds | 32.41/$nm^2$ | 51. 59/$nm^2$ |

the different planes would result in sheet morphology of $Cu_3P$ crystals with a larger (001) facet.

To further study the crystal structure of the $Cu_3P$ nanosheets in detail, EDS, XPS and HAADF-STEM were performed. EDS results confirmed the presence of only Cu and P with no other impurity element present (supplementary Fig. S2). XPS of $Cu_3P$-5 shows two peaks of phosphorus with binding energies of 129.5 and 133.18 eV (Fig. 2a). The peak at 133.18 eV indicates the presence of phosphate ($PO_x$) which might be formed on the surface of $Cu_3P$. The other peak (129.5 eV) with a lower binding energy than elemental phosphorus (130.2 eV) is attributed to phosphorous bonded to copper. These attributions are in accordance with reported XPS studies on $Cu_3P$ [22,23]. Atomic resolution HAADF-STEM image (Fig. 2b) shows that the as-grown $Cu_3P$ has no structural defects and the structure is consistent with the atomic model of $Cu_3P$ (001). The EDS, XPS and HAADF-STEM results together confirm the high crystallinity of the grown $Cu_3P$ nanosheets.

Interestingly, we observed that $Cu_3P$ sheets on Cu foil were uniformly aligned in the same direction, especially for $Cu_3P$-5 that shows a nanoarchitecture (Fig. 1b). To further verify the origin of this alignment, we considered the alignment in a $Cu_3P$ sample in the early stage of growth. supplementary Fig. S3 shows $Cu_3P$ prepared with a much lower amount of red phosphorus (0.05 g) showing a similar alignment. These observations strongly indicate that $Cu_3P$ grows epitaxially on the Cu foil.

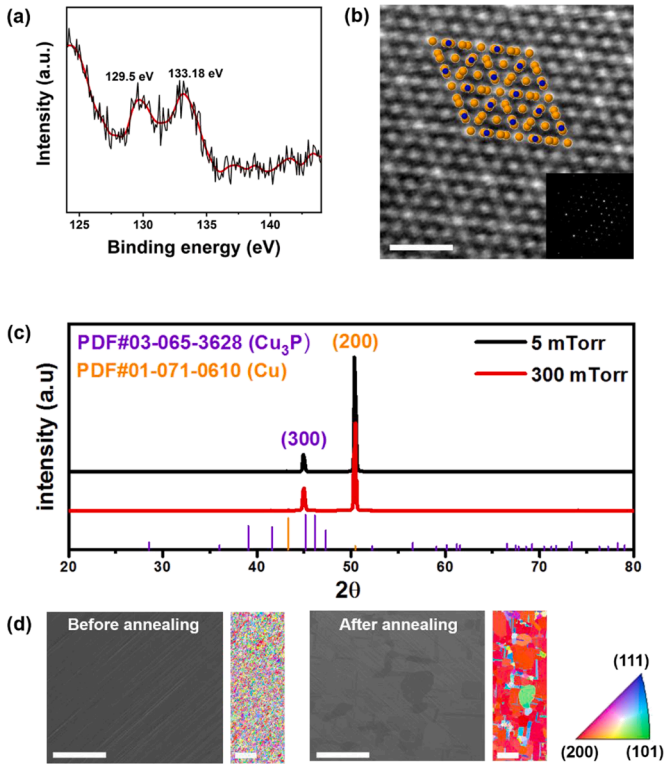


**Fig. 2.** (a) XPS of phosphorus binding energies for $Cu_3P$-5. (b) HAADF-STEM image of $Cu_3P$ nanosheets with overlaid atomic model of $Cu_3P$ (001). Scale bar is 1 nm. (c) XRD patterns of $Cu_3P$ nanoarchitectures on Cu; $Cu_3P$-5(black) and $Cu_3P$-300 (red). (d) SEM images and EBSD maps of the Cu foil surface before and after annealing at 1000 °C. Scale bars are 300 μm.

We further confirmed epitaxy from XRD. Fig. 2c shows XRD patterns of $Cu_3P$-5 and $Cu_3P$-300 on Cu foil. Only two intense peaks at the 2θ values of 44.9 ° and 50.359 °, corresponding to $Cu_3P$ (300) and Cu (200) reflections (JCPDS card Nos 03-065-3628 and 01-071-0610, respectively), are seen in both $Cu_3P$-5 and $Cu_3P$-300. This identical XRD data between $Cu_3P$- 5 and $Cu_3P$-300 indicates that they have same epitaxial relations. The bare surface of the Cu foil before and after annealing was analyzed by electron backscatter diffraction (EBSD) (Fig. 2d). Upon annealing, the Cu grain size, which was originally of the order of tens of micrometers with random orientation, grew up to hundreds of micrometers with predominantly the Cu (200) plane. Results from XRD and EBSD confirm that $Cu_3P$ sheets are epitaxially grown on Cu (200) surface.

The morphology and alignment of the nanoarchitecture was further investigated for $Cu_3P$-5 by examining the back side of the Cu foil where $Cu_3P$ nanosheets are more sparsely distributed than on the front side (since only phosphorus vapor that permeated between the quartz substrate and Cu foil was available for the reaction) (Fig. 3a). It is seen that the $Cu_3P$ nanosheets have a truncated hexagonal morphology and two characteristic features are noticeable: 1) The growth direction of the $Cu_3P$ nanosheets is always along two orthogonal directions on the Cu foil, and 2) the vertices of the truncated hexagonal $Cu_3P$ nanosheets are pointed in the same direction Next, we analyzed the interface between the $Cu_3P$ nanosheet ($Cu_3P$-5) and the Cu foil by TEM (Fig. 3b–d). Fig. 3b is a low magnification cross-sectional TEM image of $Cu_3P$ nanosheets.

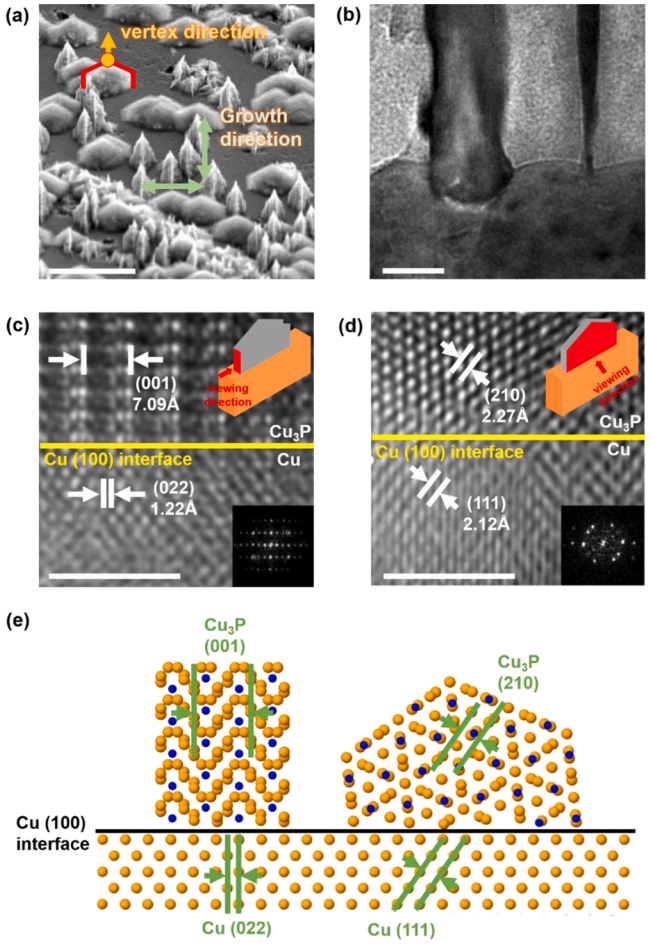


**Fig. 3.** (a) SEM image of sparsely grown $Cu_3P$ nanosheets on the backside of the Cu foil. Scale bar is 10 μm. (b) Cross-sectional TEM image of $Cu_3P$ nanosheets. Scale bar is 20 nm. (c,d) Atomic resolution TEM images of the interface between $Cu_3P$-5 and Cu at the $Cu_3P$ (c) <100> and (d) <001> zone axes. Bottom right images are digital diffractograms of the TEM images. Scale bars are 1 nm. (e) Atomic model corresponding to Fig. 3c and d.

The thicknesses of the two nanosheets are in the same range as those measured by SEM. The atomic-resolution cross-section TEM image clearly shows that a Cu (100) plane forms the interface between the $Cu_3P$ nanosheets and the Cu surface (shown by the yellow line in Fig. 3c), which is consistent with our EBSD result. In addition, the $Cu_3P$ (001) plane is aligned parallel to the Cu (022) plane. When the interface was analyzed at the <001> zone axis of $Cu_3P$ as shown in Fig. 3d, we found that here too, the Cu (100) interface is observed indicating that Cu/$Cu_3P$ interface is always the Cu (100) plane, which is consistent with EBSD results. At the $Cu_3P$ <001> zone axis, the $Cu_3P$ (210) plane is aligned to the Cu (111) plane with a 6.6% lattice mismatch. Additionally, the epitaxial relation of $Cu_3P$ (210)/Cu (111) was identically observed for $Cu_3P$-300 (supplementary Fig. S4), which clearly shows that $Cu_3P$-300 has the same epitaxial relations with $Cu_3P$-5 as mentioned in XRD results.

These interfaces point to the presence of two epitaxial relations: 1) $Cu_3P$ (001)/Cu (022) and 2) $Cu_3P$ (210)/Cu (111), which are clearly shown in the corresponding atomic model in Fig. 3e. The two epitaxial relations account for the two characteristic morphological features of the $Cu_3P$ nanosheets nanoarchitecture described in Fig. 3a. First, the $Cu_3P$ (001)/Cu (022) epitaxial relation results in the two orthogonal growth directions of $Cu_3P$ nanosheets (Fig. 3a) stemming from the two Cu {022} family of planes on the Cu (100) surface (supplementary Fig. S5). The $Cu_3P$ (210)/Cu (111) epitaxy leads to all the vertices of the truncated hexagonal $Cu_3P$ nanosheets having the same direction as shown in Fig. 3a. Due to the two epitaxial relations, the truncated hexagonal $Cu_3P$ nanosheets having the same vertex direction grow preferentially along two orthogonal directions on the Cu foil, resulting in the observed nanoarchitecture. Additionally, these two epitaxial relations are different with the previously reported relations between Cu and $Cu_3P$ [24]. The reason for that is attributed to differently formed interfaces. In our case, Cu (100) is formed as interface between Cu and $Cu_3P$, but Cu ($13\bar{3}$) and Cu (221) are formed as the interface in the previous report. Therefore, it indicates that Cu surface engineering is necessary to fabricate the nanoarchitecture of aligned $Cu_3P$ nanosheets.

Lastly, we studied the electrochemical properties of $Cu_3P$ nanoarchitecture by using it as anode in a LIB and as electrocatalyst for the HER. We elucidated the effect of the nanoarchitecture morphology ($Cu_3P$-5) by comparing its performance to $Cu_3P$ with film-like morphology ($Cu_3P$-300).

Fig. 4a shows the charge and discharge potential curves for $Cu_3P$ nanosheets nanoarchitecture ($Cu_3P$-5). The discharge curve has two obvious plateaus near 0.89 and 0.8 V, which are related to the formation of $Li_xCu_{3-x}P$ and complete conversion into $Li_3P$. In the charging curve, there are three plateaus ~ 0.72, 1.09, and 1.26 V which are related to the slow loss of lithium, conversion of $Li_3P$ into $Li_{3-x}Cu_xP$, and recovery of $Cu_3P$ [25,26]. The discharge rate capabilities for $Cu_3P$-5 (red) and $Cu_3P$-300 (blue) are compared in Fig. 4b. For the former, the discharge capacity increased from 298.4 mAh/g to 327.6 mAh/g for the first 3 cycles at 0.05 C but slowly stabilized during the following cycles. When the rate at 0.2 C was re-tested after 21 cycles, the initial capacity was restored to a value that was even slightly higher than the previous 0.2 C test. For $Cu_3P$-300 with a film-like morphology, the overall capacity was lower than for the nanoarchitecture. The higher discharge capacity of $Cu_3P$-5 even in initial cycle is due to synergistic effects of nanoarchitecture with leads to more open channels for ion transfer, electrochemical active sites, and large contact area between electrolyte and active material [27]. In addition, the capacity was further lowered with increasing cycle number in contrast to the nanoarchitecture. An optical image showing the half of a coin cell of the two $Cu_3P$ samples after rate capability test is shown in supplementary Fig. S6. The $Cu_3P$ nanoarchitecture ($Cu_3P$-5) retained its initial state after the test, but the $Cu_3P$ anode with film-like morphology ($Cu_3P$-300) was detached from the Cu foil. We attribute the stability of the nanoarchitecture to the presence of sufficient buffer space to accommodate the volume expansion occurring during charging and discharging. A film-like architecture, due to its compact nature, cannot accommodate this expansion. These results show that the nanoarchitecture has the definite advantage over the film-like morphology when using $Cu_3P$ nanosheets as a LIB anode.

We tested the electrocatalytic activity of the nanoarchitecture of $Cu_3P$ nanosheets for the HER. Fig. 5a shows HER polarization curves for $Cu_3P$ with nanoarchitecture and film morphologies. The measurement was carried out in 0.5 M $H_2SO_4$ with a scan rate 10 mV/s. In the first cycle, the nanoarchitectured $Cu_3P$ had a lower overpotential (291 mV at 10 mA/cm$^2$) compared to the film- like $Cu_3P$ (551 mV at 10 mA/cm$^2$), indicating a higher electrocatalytic activity. This higher HER performance also shows the benefits of nanoarchitecture for energy applications because the high surface area of nanoarchitecture provides more active sites between electrolyte and active materials and this leads to superior performance of nanoarchitecture. However, the HER efficiency of the nanoarchitecture degraded slightly with increasing cycling number. In contrast, the performance of the film-like $Cu_3P$ increased with cycle number and was similar to that of the nanoarchitecture at the end of 1000 cycles. This behavior is also observed in the Tafel slopes (Fig. 5b), where Tafel slope of the $Cu_3P$ nanoarchitecture was slightly changed from 83.7 to 83.1 mV/dec but that for the film-like $Cu_3P$ decreased significantly from 126.9 to 72.6 mV/dec. To explain this behavior, the morphology of the $Cu_3P$ electrodes after 1000 cycles of HER was studied using optical microscopy. The nanoarchitecture of $Cu_3P$ nanosheets suffered a drastic change in morphology after 1000 cycles with the nanoarchitecture reconstructing to form microparticles (Fig. 5c). This morphology reconstruction is evidently responsible for the decrease in HER efficiency. Interestingly, similar microparticles were observed in $Cu_3P$ with film-like morphology after 1000 cycles of

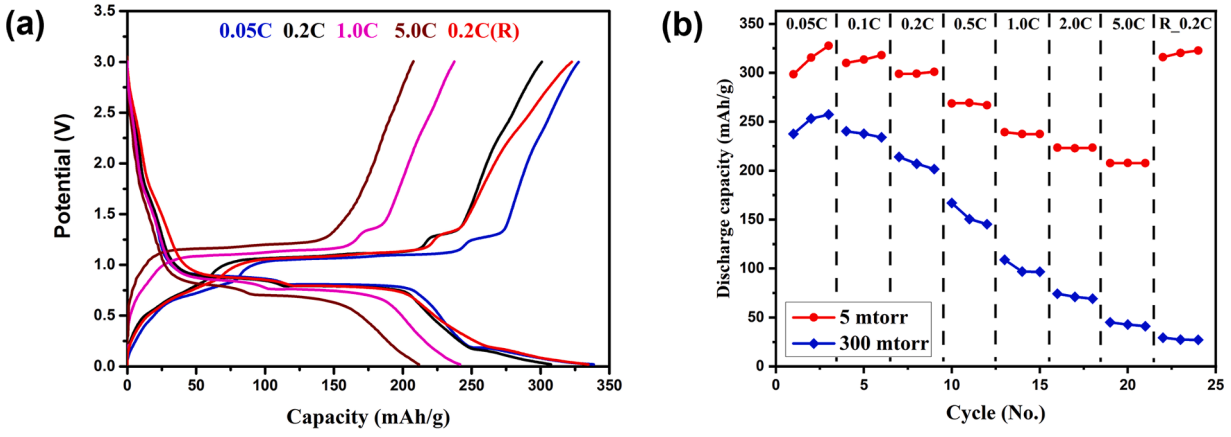


**Fig. 4.** (a) Charge and discharge voltage profiles of $Cu_3P$-5 nanoarchitecture at different rates and (b) rate capability of $Cu_3P$-5 (red) and $Cu_3P$-300 (blue).

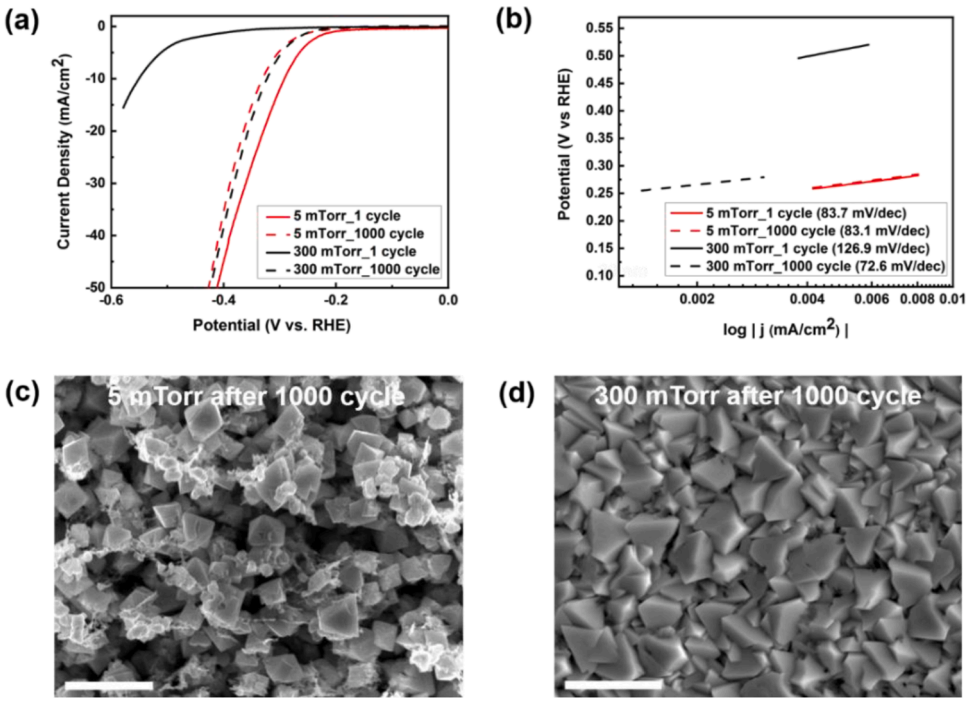


**Fig. 5.** (a) HER polarization curves and (b) Tafel plots of $Cu_3P$-5 (red) and $Cu_3P$-300 (black) pressure for 1 (solid lines) and 1000 (dash lines) cycles. (c,d) SEM images of $Cu_3P$ architectures (c) $Cu_3P$-5 and (d) $Cu_3P$-300 after 1000 cycles of HER.

HER (Fig. 5d). This suggests that $Cu_3P$ morphology undergoes reconstruction to form microparticles during HER cycling in $H_2SO_4$ solution regardless of the initial morphology.

## 4. Conclusion

In summary, this study shows that nanoarchitecture of $Cu_3P$ nanosheets can be directly fabricated with controlling the thickness of $Cu_3P$ nanosheets and substrate engineering to ensure epitaxial relations between $Cu_3P$ and the Cu foil. The thickness of $Cu_3P$ sheets was controlled from tens of nanometers to hundreds of micrometers by varying the chamber pressure during the growth. Additionally, the investigated epitaxial relations, $Cu_3P$ (001)/Cu (002) and $Cu_3P$ (210)/Cu (111), influenced the alignment of $Cu_3P$ nanosheets. The direct fabrication of nanoarchitecture $Cu_3P$ nanosheets on a Cu foil allowed to evaluate its performance as anode in a LIB. The $Cu_3P$ nanoarchitecture clearly showed higher capacity and durability in comparison with $Cu_3P$ with film-like morphology. For HER, the electrocatalytic efficiency of the nanoarchitecture was superior in the initial cycles but both morphologies showed the same performance at the end of 1000 cycles. We attribute this behavior to reconstruction of morphology of $Cu_3P$ during cycling. Our work provides a simple method for the direct fabrication of a TMPs nanoarchitecture on a current collector and highlights the effect of nanoarchitecture on the performance of TMPs in typical energy applications.

## CRediT authorship contribution statement

**Suk Woo Lee:** Conceptualization, Methodology, Investigation, Data curation, Writing – original draft. **Jaemin Kim:** Investigation, Resources, Validation. **Sang-Gil Woo:** Investigation, Resources, Formal analysis. **Youngjin Park:** Investigation, Resources, Formal analysis. **Jong Chan Yoon:** Formal analysis, Methodology. **Hyo Ju Park:** Investigation, Resources. **Na Yeon Kim:** Methodology, Validation. **Hyeon Suk Shin:** Resources. **Zonghoon Lee:** Conceptualization, Methodology, Data curation, Resources, Supervision, Project administration, Writing – review & editing.

## Declaration of Competing Interest

The authors declare that they have no known competing financial interests or personal relationships that could have appeared to influence the work reported in this paper.

## Acknowledgement

This work was supported by Institute for Basic Science (IBS-R019-D1) and the National Research Foundation of Korea (NRF) grant funded by the Korea government (MSIT) (no. 2018R1A2A2A05019598).

## Supplementary materials

Supplementary material associated with this article can be found, in the online version, at doi:10.1016/j.surfin.2021.101369.

## References

[1] K. Zhou, W.J. Zhou, L.J. Yang, J. Lu, S. Cheng, W.J. Mai, Z.H. Tang, L.G. Li, S. W. Chen, Ultrahigh-performance pseudocapacitor electrodes based on transition metal phosphide nanosheets array via phosphorization: a general and effective approach, Adv. Funct. Mater. 25 (2015) 7530–7538, https://doi.org/10.1002/adfm.201503662.
[2] M. Sun, H.J. Liu, J.H. Qu, J.H. Li, Earth-rich transition metal phosphide for energy conversion and storage, Adv. Energy. Mater. 6 (2016), 1600087, https://doi.org/10.1002/aenm.201600087.
[3] A. Han, H.Y. Zhang, R.H. Yuan, H.X. Ji, P.W. Du, Crystalline copper phosphide nanosheets as an efficient Janus catalyst for overall water splitting, ACS Appl. Mater. Interfaces 9 (2017) 2240–2248, https://doi.org/10.1021/acsami.6b10983.
[4] M. Liu, R. Zhang, L. Zhang, D. Liu, S. Hao, G. Du, A.M. Asiri, R. Kong, X. Sun, Energy-efficient electrolytic hydrogen generation using Cu3P nanoarray as a bifunctional catalyst for hydrazine oxidation and water reduction, Inorg. Chem. Front. 4 (2017) 420–423, https://doi.org/10.1039/C6QI00384B.
[5] C. Villevieille, F. Robert, P.L. Taberna, L. Bazin, P. Simon, L. Monconduit, The good reactivity of lithium with nanostructured copper phosphide, J. Mater. Chem. 18 (2008) 5956–5960, https://doi.org/10.1039/B810841B.
[6] D. Yang, J.X. Zhu, X.H. Rui, H.T. Tan, R. Cai, H.E. Hoster, D.Y.W. Yu, H.H. Hng, Q. Y. Yan, Synthesis of cobalt phosphides and their application as anodes for lithium ion batteries, ACS Appl. Mater. Interfaces 5 (2013) 1093–1099, https://doi.org/10.1021/am302877q.
[7] H.J. Zhang, Y.Y. Feng, Y. Zhang, L. Fang, W.X. Li, Q. Liu, K. Wu, Y. Wang, Peapod-like composite with nickel phosphide nanoparticles encapsulated in carbon fibers

as enhanced anode for Li-ion batteries, ChemSusChem 7 (2014) 2000–2006, https://doi.org/10.1002/cssc.201301394.
[8] Y.M. Shi, B. Zhang, Recent advances in transition metal phosphide nanomaterials: synthesis and applications in hydrogen evolution reaction, Chem. Soc. Rev. 45 (2016) 1529–1781, https://doi.org/10.1039/C5CS00434A.
[9] J.H. Hao, W.S. Yang, Z.P. Huang, C. Zhang, Superhydrophilic and superaerophobic copper phosphide microsheets for efficient electrocatalytic hydrogen and oxygen evolution, Adv. Mater. Interfaces 3 (2016), 1600236, https://doi.org/10.1002/admi.201600236.
[10] C.G. Read, J.F. Callejas, C.F. Holder, R.E. Schaak, General strategy for the synthesis of transition metal phosphide films for electrocatalytic hydrogen and oxygen evolution, ACS Appl. Mater. Interfaces 8 (2016) 12798–12803, https://doi.org/10.1021/acsami.7b02069.
[11] J.W. Qin, Q. Zhang, Z.Y. Cao, X. Li, C.W. Hu, B.Q. Wei, MnOx/SWCHT macro-films as flexible binder-free anodes for high-performance Li-ion batteries, Nano Energy 2 (2013) 733–741, https://doi.org/10.1016/j.nanoen.2012.12.009.
[12] B. Rajagopalan, B. Kim, S.H. Hur, J.S. Chung, Alternative binder-free electrode based on facile deposition of carbon/graphene-$TiO_2$ on the coin cell anode for a lithium-ion battery, Surf. Coat. Tech. 315 (2017) 359–367, https://doi.org/10.1016/j.surfcoat.2017.02.064.
[13] J. Cabana, L. Monconduit, D. Larcher, M.R. Palacin, Beyond intercalation-based Li-ion batteries: the state of the art and challenges of electrode materials reacting through conversion reactions, Adv. Mater. 22 (2010) E170–E192, https://doi.org/10.1002/adma.201000717.
[14] L. Yue, J. Liang, Z. Wu, B. Zhong, Y. Luo, Q. Liu, T. Li, Q. Kong, Y. Liu, A.M. Asiri, X. Guo, X. Sun, Progress and perspective of metal phosphide/carbon heterostructure anodes for rechargeable ion batteries, J. Mater. Chem. A 9 (2021) 11879–11907, https://doi.org/10.1039/D1TA01626A.
[15] S.B. Yang, Y.J. Gong, J.S. Zhang, L. Zhan, L.L. Ma, Z.Y. Fang, R. Vajtai, X.C. Wang, P.M. Ajayan, Exfoliated graphitic carbon nitride nanosheets as efficient catalysts for hydrogen evolution under visible light, Adv. Mater. 25 (2013) 2452–2456, https://doi.org/10.1002/adma.201204453.
[16] Z.B. Chen, D. Cummins, B.N. Reinecke, E. Clark, M.K. Sunkara, T.F. Jaramillo, Core-shell $MoO_3$-$MoS_2$ Nanowires for hydrogen evolution: a functional design for electrocatalytic materials, Nano Lett. 11 (2011) 4168–4175, https://doi.org/10.1021/nl2020476.
[17] E.J. Popczun, C.G. Read, C.W. Roske, N.S. Lewis, R.E. Schaak, Highly active electrocatalysis of the hydrogen evolution reaction by cobalt phosphide nanoparticles, Angew. Chem. Int. Ed. 53 (2014) 5427–5430, https://doi.org/10.1002/anie.201402646.
[18] J.Y. Xiang, X.L. Wang, J. Zhong, D. Zhang, J.P. Tu, Enhanced rate capability of multi-layered ordered porous nickel phosphide film as anode for lithium ion batteries, J. Power Sources 196 (2011) 379–385, https://doi.org/10.1016/j.jpowsour.2010.06.068.
[19] H. Wang, X.Z. Xu, J.Y. Li, L. Lin, L.Z. Sun, X. Sun, S.L. Zhao, C.W. Tan, C. Chen, W. H. Dang, H.Y. Ren, J.C. Zhang, B. Deng, A.L. Koh, L. Liao, N. Kang, Y.L. Chen, H. Q. Xu, F. Ding, K.H. Liu, H.L. Peng, Z.F. Liu, Surface monocrystallization of copper foil for fast growth of large single-crystal graphene under free molecular flow, Adv. Mater. 28 (2016) 8968–8974, https://doi.org/10.1002/adma.201603579.
[20] K. Hiramatsu, K. Nishiyama, A. Motogaito, H. Miyake, Y. Iyechika, T. Maeda, Recent progress in selective area growth and epitaxial lateral overgrowth of III-nitrides: effects of reactor pressure in MOVPE growth, Phys. Stat. Sol. A 176 (1999) 535–543, https://doi.org/10.1002/(SICI)1521-396X(199911)176:1<535::AID-PSSA535>3.0.CO;2-I.
[21] G. Manna, R. Bose, N. Pradhan, Semiconducting and plasmonic copper phosphide platelets, Angew. Chem. Int. Ed. 52 (2013) 6762–6766, https://doi.org/10.1002/anie.201210277.
[22] Z.Z. Li, Y.M. Xin, W.L. Wu, B.L. Fu, Z.H. Zhang, Topotactic conversion of copper(I) phosphide nanowires for sensitive electrochemical detection of $H_2O_2$ release from living cells, Anal. Chem. 88 (2016) 7724–7729, https://doi.org/10.1021/acs.analchem.6b01637.
[23] Y.C. Chen, Z.B. Chen, Y.G. Lin, Y.K. Hsu, Synthesis of copper phosphide nanotube arrays as electrodes for asymmetric supercapacitors, ACS Sustain. Chem. Eng. 5 (2017) 3863–3870.
[24] L. De Trizio, A. Figuerola, L. Manna, A. Genovese, C. George, R. Brescia, Z. Saghi, R. Simonutti, M. Van Huis, A. Falqui, Size-tunable, hexagonal plate-like $Cu_3P$ and Janus-like Cu-$Cu_3P$ nanocrystals, ACS Nano 6 (2012) 32–41, https://doi.org/10.1021/nn203702r.
[25] B. Mauvernay, M.L. Doublet, L. Monconduit, Redox mechanism in the binary transition metal phosphide $Cu_3P$, J. Phys. Chem. Solids 67 (2006) 1252–1257, https://doi.org/10.1016/j.jpcs.2006.01.055.
[26] S.B. Ni, J.J. Ma, X.H. Lv, X.L. Yang, L.L. Zhang, The fine electrochemical performance of porous $Cu_3P$/Cu and the high energy density of $Cu_3P$ as anode for Li-ion batteries, J. Mater. Chem. A 2 (2014) 20506–20509, https://doi.org/10.1039/C4TA03871A.
[27] F. Fu. Y. Yao, H. Wang, G.-L. Xu, K. Amine, S.-G. Sun, M. Shao, Structure dependent electrochemical performance of Li-rich layered oxides in lithium-ion batteries, Nano Energy 35 (2017) 370–378, https://doi.org/10.1016/j.nanoen.2017.04.005.